Optimized Phase-Retrieval Technique for Coherent Diffractive Microscopy: Guided Ptychography Iterative Engine

Cheng-Wei Hsu, Ping Lu, Pei-Chi Huang, Jia-Ru Yu, Chi Chen, Shang- Da Yang, and Chien-Chun Chen

***Abstract*—We have developed a guided ptychography iterative engine (gPIE) algorithm that applies the concept of optimization to the conventional ePIE (extended ptychography iterative engine) approach. Instead of accessing a random or spiral trajectory among the collected diffraction patterns to implement the phase-retrieval, gPIE guides the searching direction through the local minimum and minimizes the cost function, which is the difference between the calculated intensities and the experimental ones, to approach the global minimum. Compared with ePIE, gPIE robustly reconstructs a more accurate sample and illumination, thus revealing the correct surface topology. The feasibility of gPIE was verified experimentally by acquiring sequential diffraction patterns from a UV laser.**

***Index Terms*—Coherent imaging, diffractive imaging, microscopy, phase-retrieval algorithm.**

I. Introduction

COHERENT diffraction imaging (CDI) has drawn significant attention in the fields of nano- and bio-imaging due to the potential of imaging macromolecules without crystallization [1]–[7]. Compared to the image quality in conventional microscopy, which usually suffers from low numerical aperture (NA) and astigmatism, this lens-less technique reconstructs the missing phases directly from the diffraction pattern to guarantee the best image resolution [8]–[12]. This feature is particularly desirable in the short wavelength (e.g., EUV or x-ray) region as the high-quality optics are not easily accessible.

Manuscript received 2 June 2022; revised 29 June 2022; accepted 2 July 2022. Date of publication 5 July 2022; date of current version 12 July 2022. This work was supported by the Taiwan Ministry of Science and Technology under Grants 109-2112-M-007-029-MY3 and 110-2119-M-007-002-MBK. *(Cheng-Wei Hsu and Ping Lu contributed equally to this work.) (Corresponding author: Chien-Chun Chen.)*

Cheng-Wei Hsu and Shang- Da Yang are with the Institute of Photonics Technologies, National Tsing Hua University, Hsinchu 30013, Taiwan (e-mail: cwhsu0726@gmail.com; sdyang@ee.nthu.edu.tw).

Ping Lu is with the Department of Engineering and System Science, National Tsing Hua University, Hsinchu 30013, Taiwan (e-mail: byepjlu@gmail.com).

Chien-Chun Chen is with the Department of Engineering and System Science, National Tsing Hua University, Hsinchu 30013, Taiwan, and also with National Applied Research Laboratories, Taiwan Instrument Research Institute, Hsinchu 30076, Taiwan (e-mail: chenchienchun0627@gmail.com).

Pei-Chi Huang is with the R&D Division, BrightEST Company Ltd., Hsinchu County 31061, Taiwan (e-mail: pchuang@brightest-euv.com).

Jia-Ru Yu and Chi Chen are with the Research Center for Applied Sciences, Academia Sinica, Taipei 11529, Taiwan (e-mail: puddingdes@gmail.com; chenchi@gate.sinica.edu.tw).

Digital Object Identifier 10.1109/JPHOT.2022.3188574

However, CDI was found less practical since it requires a well-constrained sample region to satisfy the Nyquist oversampling rate [13]–[15]. Such a constraint limits the examination's field of view (FOV) and heavily narrows the applicable scenarios. Ptychography bypasses the restriction by producing sufficient data redundancy, scanning the sample with a finite illumination of a suitable overlapping ratio [16]–[19].

Although the ptychographic approach allows the exploration of non-isolated specimens, it is not trivial to obtain robust reconstructions of both object and probe images from noisy diffraction data [20]. For instance, the reconstruction might be trapped in local minima due to the phase problem [21]; therefore, varying the initial guesses may produce inconsistent results and introduce artifacts. In addition, the sequence of individual diffraction patterns adopted into the iteration process dramatically affects the convergence of the reconstruction [22]. Prior information on the illumination wavefront and abundant knowledge of the optical elements used in experiments can generate an excellent initial guess [23], [24]. Nevertheless, a systematic approach to optimizing the iterative trajectory is still desired for the existing studies. In this work, we adapted a paradigm shift of the guiding concept from the guided hybrid input-output method (GHIO) [25] to optimize the conventional ePIE [26] for the aforementioned issue. By reconstructing a UV laser diffraction experiment, we have demonstrated that the gPIE algorithm is immune to the ambiguity caused by changing the iterative trajectory and guarantees the convergence in reflected ptychography.

II. Method

Following the basic concept of the ePIE method, we start with an initial guess for the Probe (P) and object (O) wavefronts. The diffraction patterns $j = 1,2,3,\ldots, J$ concerning the illumination across the object through a raster trajectory are recorded by the camera in sequence, where J is the total number of diffraction patterns. Generally, it is necessary to process the diffraction patterns in a specific order, such as a random or a spiral sequence. The exit wave function $\psi_j(r)$ at position r_j is first calculated by multiplying the current object and probe, as shown in (1). We propagate this exit wave to the far-field detector plane by applying the Fourier transform, obtaining the diffractive waves $\psi_j(q)$, as (2).

$$\psi_j(r) = P(r - r_j)\, O(r). \tag{1}$$

$$\psi_j(q) = \mathcal{F}[\psi_j(r)]. \tag{2}$$

To enforce the consistency with collected diffraction patterns, the amplitudes of the diffractive waves $\psi_j(q)$ is then replaced with the square root of the measured intensities, as (3). An inverse Fourier transform is then performed to update the exit wave function, as (4).

$$\psi'_j(q) = \sqrt{I_j(q)}\frac{\psi_j(q)}{|\psi_j(q)|}. \tag{3}$$

$$\psi'_j(r) = \mathcal{F}^{-1}[\psi'_j(q)]. \tag{4}$$

Finally, the object and probe functions are revised by (5) and (6), where α and β are numbers between 0 and 1.

$$O'(r) = O(r) + \alpha\frac{P^*(r - r_j)}{|P(r - r_j)|^2_{max}}[\psi'_j(r) - \psi_j(r)], \tag{5}$$

$$P'(r) = P(r) + \beta\frac{O^*(r + r_j)}{|O(r + r_j)|^2_{max}}[\psi'_j(r) - \psi_j(r)]. \tag{6}$$

To quantitatively determine the reconstruction quality, an error function *erf K* measuring the difference between the reconstructed amplitudes and the collected ones is defined as (7),

$$erf\ K = \sum_{j=1}^{J}\frac{\sum_{q\in D}\left||\psi_j(q)| - \sqrt{I_j(q)}\right|}{\sum_{q\in D}\sqrt{I_j(q)}}, \tag{7}$$

where $q \in D$ presents the area of collected diffraction patterns. Although the ePIE algorithm is well-known for producing successful reconstructions in several cases, the reconstruction quality can still severely deteriorate. For example, random updating order during the ePIE iteration often causes a high *erf K*, and artifacts when different initial conditions are employed. The proposed gPIE differs ePIE in two aspects: First, we adapt numbers of ePIE with varying updating orders. Second, refine the objects and probes with the reconstructed object and probe with the lowest *erf K* every *g* iteration, taking the guided guesses as to the initial condition for the next iteration. The detailed steps of gPIE are as follows: (i) Assigning the *N* random updating trajectories (i.e., seeds). (ii) Starting the ePIE algorithm with *g* iterations (defined as one generation, e.g., $g = 50$) for each seed. (iii) After one generation is accomplished, choosing the object with the smallest *erf K* as the guiding reference, denoted as $O^{g,best}$ and $P^{g,best}$, respectively. (iv) Refining reconstructed objects and probes from the other seeds by (8) and (9),

$$O^{g+1,\,s}(r) = \left[O^{g,best}(r) \times O^{g,s}(r)\right]^{\frac{1}{2}}, \tag{8}$$

$$P^{g+1,\,s}(r) = \left[P^{g,best}(r) \times P^{g,s}(r)\right]^{\frac{1}{2}}, \tag{9}$$

where *s* is the *s*-th seed. (v) Repeating the step (ii)∼(v) until the error becomes stagnated. Fig. 1 illustrates the flowchart of the gPIE algorithm.

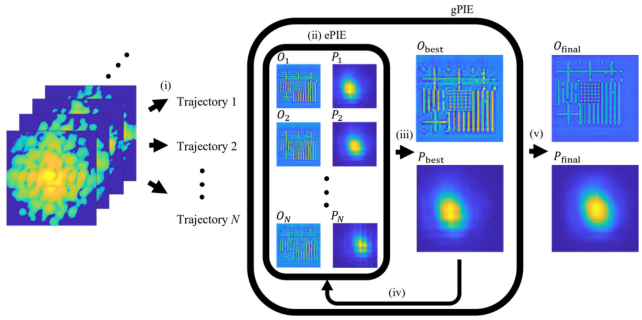

Fig. 1. Flowchart of guiding ptychography iterative engine (gPIE). (i) The updating trajectory of collected diffraction patterns of each seed is randomly arranged before starting iteration. (ii) Executing conventional ePIE to obtain individual reconstructions. (iii) Selecting the object and probe of a seed with the smallest *erf K* value as the reference. (iv) Guiding the object and probe of each seed via geometry mean with the reference after a generation is completed. (v) After several generations, we obtain the final reconstruction result with the smallest *erf K*.

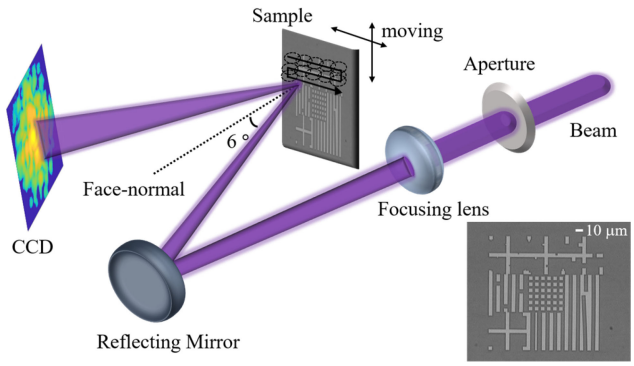

Fig. 2. Schematic layout of reflection-mode ptychography experimental setup. The 343 nm UV beam propagates through an aperture and is focused by the focusing lens ($f = 15$ cm) onto the sample at an angle of incidence of 6 degrees. A CMOS camera records the signal of scattered light at a distance of 26.5 mm. Micrograph of the sample is shown in the lower right corner.

III. Experiment

The experimental beamline used for gPIE is shown in Fig. 2, including a coherent light source, a focus lens, a reflecting mirror, and a nanopositioning stage. The laser system provides laser beams with a wavelength of 343 nm and is focused by the focusing lens ($f = 15$ cm) into the experimental enclosure. The mirror reflects the beam onto the sample at an angle of incidence of 6 degrees. The sample consisting of about 70 nm thick chromium patterned on a sapphire substrate is mounted on the 2-axis nanopositioning stage and illuminated by the focused probe with a ∼20 mm diameter. As shown in Fig. 2, the stage steps in a raster trajectory with a 10 mm step size correspond to around a 50% overlapping ratio. The reflective diffraction signals of the adjacent areas on the sample are recorded by a 12-bits, 5.2M pixels scientific-grade CMOS camera at a distance of 26.5 mm, resulting in a numerical aperture (NA) of 0.08. To increase the dynamic range of the diffraction signals, we perform the high dynamic range (HDR) technique by taking three images with different exposure periods (1, 5, and 20 ms) at each position with no saturation pixels in the data obtained by the shortest

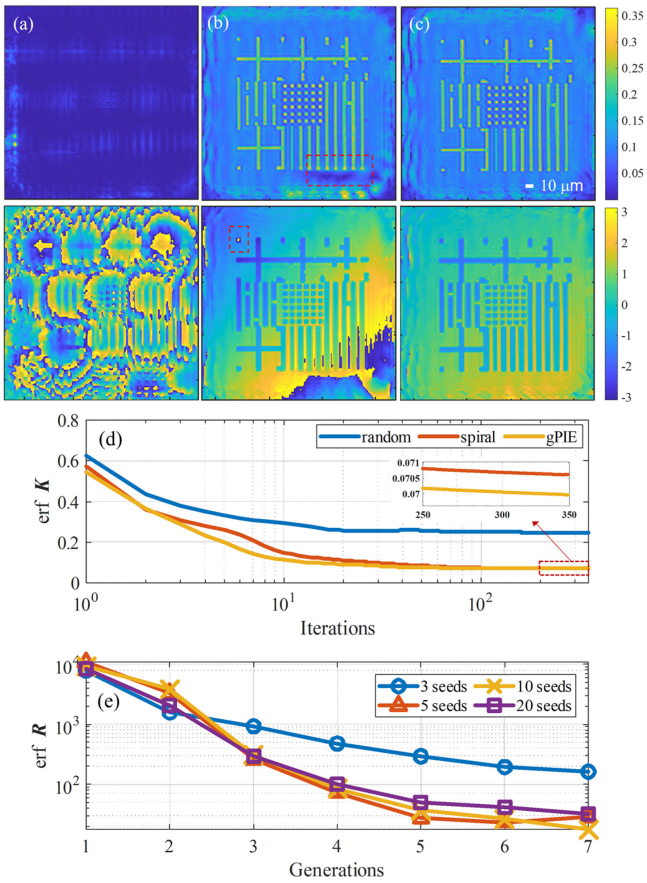

Fig. 3. Ptychographic reconstruction, error function of Fourier space (*erf K*), and error function of real space (*erf R*). The reconstructed image by ePIE and gPIE with three different update trajectories in (a–c). The upper row presents amplitude; the lower row presents phase. (a) ePIE-Random trajectory. (b) ePIE-Spiral trajectory. The red-dash rectangle indicates the amplitude and phase artifacts (c) gPIE-10seeds. (d) Comparison of *erf K* between three different trajectories. (e) Evolution of *erf R* with a different number of seeds.

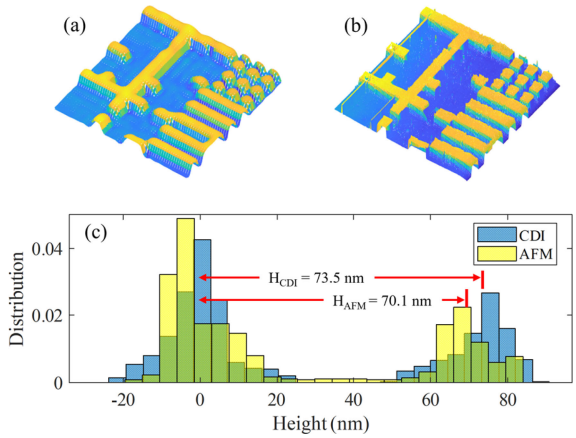

Fig. 4. Surface profile comparison between AFM and gPIE. (a) Surface information of the object based on UV measurement using gPIE reconstruction and (b) Surface information of the object using AFM measurement. (c) Histograms of the surface profile. The histogram is used to calculate the average height of the substrate and deposited chromium for both CDI and AFM measurements.

exposure time. Additionally, the collected diffraction data is then zero-padded to double the pixel resolution in real space. Note that the optical resolution does not change by this procedure as it only plays a role of interpolation in real space equivalently.

IV. Results and Discussions

The reconstructed images are shown in Fig. 3. The random iterative trajectories cannot guarantee successful reconstructions and might get trapped in a local minimum. The spiral trajectory seems to be a more reliable path as the probes are sufficiently overlapped with their adjacent regions at the beginning of the iteration, leading to a more vital constraint and faster convergence. However, the object amplitude and phase reconstructed in the case of the spiral trajectory still show significant artifacts. In contrast, the artifacts are significantly alleviated in the image reconstructed by gPIE with 10 seeds. Compared to ePIE with a random and spiral iterative trajectory, gPIE achieves convergence faster, leading to lower error metrics, as shown in Fig. 3(d). It should be noted that only the error of the optimal seed is figured for simplicity. We also investigate the number of seeds that seem to play an essential role in directing the optimal. Although the reconstruction should benefit from increasing the number of seeds, an immoderately increasing of seeds apparently degrade the computing efficiency as the computation time is proportional to the number of seeds. We test the gPIE algorithm on the same data but with 3, 5, 10, and 20 seeds and calculate the accumulated difference among all reconstructed objects versus the average object at each generation to monitor the degree of convergence,

$$\bar{O}^g(r) = \sum_{s=1}^{N} \frac{O^{g,s}(r)}{N}. \tag{10}$$

$$erf\ R = \frac{1}{N}\sum_{s=1}^{N}\sum_{r}\left|\frac{\left|\bar{O}^g(r)\right| - \left|O^{g,s}(r)\right|}{\left|\bar{O}^g(r)\right|}\right|. \tag{11}$$

Due to the linear phase ambiguity [27], the position of the reconstructed objects may exhibit an arbitrary shift for different seeds, so we align the objects with their density center before examining the difference. As shown in Fig. 3(e), the cases of 5, 10, and 20 seeds converge to a similar *erf R* after seven generations, implying that gPIE very likely lead the convergence direction to a global minimum instead of a local minimum when the number of seeds is more enough.

We now employ gPIE to reconstruct both the object and probe robustly. Therefore, we can obtain surface topology from the phase of the reconstructed object [28], [29]. The surface profile can be obtained by calculating the reflecting phase shifts and the optical path difference between the substrate and the chromium $2h/\cos\theta$, where h is the thickness of the deposited chromium. By taking the reflecting phase shift φ_s and φ_c from the sapphire substrate and deposited chromium into account, the overall phase shift is $\Delta\phi = -2kh/\cos\theta - \varphi_s + \varphi_c$. A polynomial subtraction is first applied on the reconstructed phase map to remove the trend before extracting the height information. This analysis is rendered as a 3D height map in Fig. 4(a), where φ_s and φ_c have been taken by 0 and $\pi/6$ according to the database at 343

nm [30]. The atomic force microscopy (AFM) [31] measurement is also conducted after the ptychography reconstruction for verification, and the result is shown in Fig. 4(b). Both figures are zoomed into the same field of view to have a better visual comparison. The average height obtained from ptychography solved by gPIE is 73.5 nm, while the height is measured by 70.1 nm from AFM. The absolute error of 3.4 nm only represents an error $\sim$0.01 λ, and is expected to be improved by applying a shorter wavelength.

V. Conclusion

In this work, we have developed a new gPIE algorithm based on conventional ePIE to improve the reconstructed image quality and convergence. The algorithm demonstrated on the experimental data significantly reduces the artifact due to arbitrary or specific iterative trajectories and guarantees convergence. Furthermore, the obtained slight fluctuation among the reconstructions indicates that the uncertainty of the algorithm-based imaging technique is largely suppressed by the gPIE algorithm, improving CDI's reliability for future industrial applications.

Acknowledgment

The authors thank Dr. A. H. Kung for his technical comments to this research.

References

[1] J. Cederquist, J. Fienup, J. Marron, and R. Paxman, "Phase retrieval from experimental far-field speckle data," *Opt. Lett.,* vol. 13, no. 8, pp. 619–621, 1988.

[2] J. Miao, P. Charalambous, J. Kirz, and D. Sayre, "Extending the methodology of X-ray crystallography to allow imaging of micrometre-sized non-crystalline specimens," *Nature,* vol. 400, no. 6742, pp. 342–344, 1999.

[3] R. Neutze, R. Wouts, D. Van der Spoel, E. Weckert, and J. Hajdu, "Potential for biomolecular imaging with femtosecond X-ray pulses," *Nature,* vol. 406, no. 6797, pp. 752–757, 2000.

[4] I. K. Robinson, I. A. Vartanyants, G. Williams, M. Pfeifer, and J. Pitney, "Reconstruction of the shapes of gold nanocrystals using coherent X-ray diffraction," *Phys. Rev. Lett.,* vol. 87, no. 19, 2001, Art. no. 195505.

[5] H. N. Chapman and K. A. Nugent, "Coherent lensless X-ray imaging," *Nature Photon.,* vol. 4, no. 12, pp. 833–839, 2010.

[6] H. N. Chapman *et al.*, "Femtosecond X-ray protein nanocrystallography," *Nature,* vol. 470, no. 7332, pp. 73–77, 2011.

[7] C. Song *et al.*, "Analytic 3D imaging of mammalian nucleus at nanoscale using coherent X-rays and optical fluorescence microscopy," *Biophys. J.,* vol. 107, no. 5, pp. 1074–1081, 2014.

[8] R. W. Gerchberg, "A practical algorithm for the determination of phase from image and diffraction plane pictures," *Optik,* vol. 35, pp. 237–246, 1972.

[9] J. R. Fienup, "Reconstruction of an object from the modulus of its Fourier transform," *Opt. Lett.,* vol. 3, no. 1, pp. 27–29, 1978.

[10] J. R. Fienup, "Phase retrieval algorithms: A comparison," *Appl. Opt.,* vol. 21, no. 15, pp. 2758–2769, 1982.

[11] S. Marchesini, "Invited article: A unified evaluation of iterative projection algorithms for phase retrieval," *Rev. Sci. Instrum.,* vol. 78, no. 1, 2007, Art. no. 011301.

[12] M. Born and E. Wolf, *Principles of Optics: Electromagnetic Theory of Propagation, Interference and Diffraction of Light*. Amsterdam, The Netherlands: Elsevier, 2013.

[13] J. Miao, D. Sayre, and H. Chapman, "Phase retrieval from the magnitude of the Fourier transforms of nonperiodic objects," *JOSA A,* vol. 15, no. 6, pp. 1662–1669, 1998.

[14] J. Miao, J. Kirz, and D. Sayre, "The oversampling phasing method," *Acta Crystallographica Sect. D: Biol. Crystallogr.,* vol. 56, no. 10, pp. 1312–1315, 2000.

[15] K. Nugent, A. Peele, H. Chapman, and A. Mancuso, "Unique phase recovery for nonperiodic objects," *Phys. Rev. Lett.,* vol. 91, no. 20, 2003, Art. no. 203902.

[16] J. M. Rodenburg and H. M. Faulkner, "A phase retrieval algorithm for shifting illumination," *Appl. Phys. Lett.,* vol. 85, no. 20, pp. 4795–4797, 2004.

[17] H. M. L. Faulkner and J. Rodenburg, "Movable aperture lensless transmission microscopy: A novel phase retrieval algorithm," *Phys. Rev. Lett.,* vol. 93, no. 2, 2004, Art. no. 023903.

[18] J. M. Rodenburg, "Ptychography and related diffractive imaging methods," *Adv. Imag. Electron. Phys.,* vol. 150, pp. 87–184, 2008.

[19] P. Thibault, M. Dierolf, A. Menzel, O. Bunk, C. David, and F. Pfeiffer, "High-resolution scanning X-ray diffraction microscopy," *Science,* vol. 321, no. 5887, pp. 379–382, 2008.

[20] P. Thibault, M. Dierolf, O. Bunk, A. Menzel, and F. Pfeiffer, "Probe retrieval in ptychographic coherent diffractive imaging," *Ultramicroscopy,* vol. 109, no. 4, pp. 338–343, 2009.

[21] A. Huiser and P. V. Toorn, "Ambiguity of the phase-reconstruction problem," *Opt. Lett.,* vol. 5, no. 11, pp. 499–501, 1980.

[22] B. Salahieh, "Reflective mode Fourier ptychography," M.S. thesis, Opt. Sci., Univ. Arizona, Tucson, AZ, USA, 2015.

[23] D. F. Gardner *et al.*, "Subwavelength coherent imaging of periodic samples using a 13.5 nm tabletop high-harmonic light source," *Nature Photon.,* vol. 11, no. 4, pp. 259–263, 2017.

[24] M. Kim, S. Kim, and S. Kim, "Optical bistability based on hyperbolic metamaterials," *Opt. Exp.,* vol. 26, no. 9, pp. 11620–11632, 2018.

[25] C.-C. Chen, J. Miao, C. Wang, and T. Lee, "Application of optimization technique to noncrystalline X-ray diffraction microscopy: Guided hybrid input-output method," *Phys. Rev. B,* vol. 76, no. 6, 2007, Art. no. 064113.

[26] A. M. Maiden and J. M. Rodenburg, "An improved ptychographical phase retrieval algorithm for diffractive imaging," *Ultramicroscopy,* vol. 109, no. 10, pp. 1256–1262, 2009.

[27] O. Bunk, M. Dierolf, S. Kynde, I. Johnson, O. Marti, and F. Pfeiffer, "Influence of the overlap parameter on the convergence of the ptychographical iterative engine," *Ultramicroscopy,* vol. 108, no. 5, pp. 481–487, 2008.

[28] M. D. Seaberg *et al.*, "Tabletop nanometer extreme ultraviolet imaging in an extended reflection mode using coherent Fresnel ptychography," *Optica,* vol. 1, no. 1, pp. 39–44, Jul. 2014.

[29] B. Zhang *et al.*, "High contrast 3D imaging of surfaces near the wavelength limit using tabletop EUV ptychography," *Ultramicroscopy,* vol. 158, pp. 98–104, 2015.

[30] P. Johnson and R. Christy, "Optical constants of transition metals: Ti, V, Cr, Mn, Fe, Co, Ni, and Pd," *Phys. Rev. B,* vol. 9, no. 12, 1974, Art. no. 5056.

[31] G. Binnig, C. F. Quate, and C. Gerber, "Atomic force microscope," *Phys. Rev. Lett.*, vol. 56, no. 9, 1986, Art. no. 930.